

Enhanced photocatalytic performance of Bi_2MoO_6 via strain engineering through collaborative optimization of indium doping and oxygen vacancies

Xinyue Chang, Jiayu Liu, Zhiyuan Guo, Yanan Cheng, Qishe Yan*, Yan-Yang Li*

Green Catalysis Center, and College of Chemistry, Zhengzhou University, Henan 450001, China



ARTICLE INFO

Keywords:
Strain engineering
Indium doping
Oxygen vacancies
 Bi_2MoO_6
Photocatalysis

ABSTRACT

Investigating lattice strain manipulation as an emerging strategy for improved photocatalysis, we introduce lattice strain into Bi_2MoO_6 nanosheets through synergistic indium doping and oxygen vacancies (OVs). Structural analysis reveals distinct compressive and tensile effects induced by indium doping and OVs, respectively, leading to localized lattice strain intensification. The optimized photocatalyst displays significantly enhanced tetracycline, ciprofloxacin, oxytetracycline, and norfloxacin removal activity due to increased active sites and improved charge carrier separation efficiency induced by lattice strain. Elucidation of tetracycline cleavage pathways and assessment of intermediate molecule toxicity are presented. This collaborative approach, merging doping and OVs for lattice strain induction, provides crucial insights for advancing bismuth-based photocatalysts.

1. Introduction

The use of pharmaceuticals and personal care products (PPCPs) has proliferated across diverse domains with the progression of society and simultaneous improvement in material living standards. This surge in PPCP usage has led to the increased release of unmetabolized and untreated PPCPs into aquatic ecosystems, precipitating severe consequences for both human well-being and ecological equilibrium [1–3]. It is crucial to note that antibiotics, notably β -Lactams, tetracyclines, sulfonamides, and quinolones, emerge as quintessential exemplars within this intricate paradigm. Due to their protracted resistance to metabolism within living organisms, these antibiotics exert a pronounced influence on the conduct, reproductive proclivities, and growth dynamics of the resident organisms [4,5]. Therefore, the conception of advanced technologies engineered for the eradication of PPCPs in wastewater stands as an imperative endeavor. Among the panoply of available approaches, photocatalytic technology emerges as a preeminent strategy distinguished by its attributes of heightened efficacy, potent oxidative capabilities, environmental sustainability, and economic viability [6–8]. The pivotal juncture toward the practical realization of photocatalysis hinges on the systematic exploration and rational design of exceptional photocatalysts [9].

Within the Aurivilius oxide family, Bismuth Molybdate (Bi_2MoO_6) emerges as a material of significant interest, primarily due to its unique stratified structure arranged by $[\text{BiO}]^+ \cdot [\text{MoO}_4]^{2-} \cdot [\text{BiO}]^+$, coupled with

attributes such as cost-effectiveness, eco-friendliness, responsiveness to visible light, and robust photocatalytic stability [2,10–14]. The photocatalytic efficacy of Bi_2MoO_6 can be notably augmented through the induction of lattice imperfections [15–18]. Predominantly, this enhancement is achieved via the incorporation of oxygen vacancies (OVs) and the process of doping, both categorized as point defects. OVs are instrumental in photocatalysis, substantially impacting the electronic configuration and surface characteristics of photocatalyst, thereby promoting charge dissociation, bolstering light absorption, and amplifying surface reactivity [19]. Doping modifies the band structure of photocatalytic materials by introducing impurity energy levels, thereby broadening the spectrum of light absorption and facilitating the segregation of photogenerated electron-hole pairs. Notably, Indium ions (In^{3+}) are recognized as efficacious dopants for Bi_2MoO_6 , owing to their compatible ionic radius and valence state, permitting a direct substitution for Bi^{3+} ions within the $[\text{BiO}]^+$ layers [16]. It is imperative to acknowledge that both types of point defects inherently induce lattice strain. Nevertheless, the influence of lattice strain on photocatalytic activity remains insufficiently explored, potentially attributed to the low strain levels and the complex interplay between defect formation and strain [20].

Strain engineering emerges as a nascent yet potent methodology for augmenting photocatalytic efficacy [20]. The lattice strain can serve as a means to regulate energy band structure, modulate photogenerated carrier mobility, and coordinate surface catalytic processes.

* Corresponding authors.

E-mail addresses: qisheyanzzu@163.com (Q. Yan), yyli@zzu.edu.cn (Y.-Y. Li).

Experimental endeavors to integrate strain within photocatalysts have yielded some notable insights [21]. For instance, the investigations of Zhang et al. [22–24] shed light on the exemplary photocatalytic proficiency of layered-double hydroxide and TiO_2 nanosheets, enriched with OVs, in the context of dinitrogen fixation. The pronounced activity observed was, in part, ascribed to the lattice strain introduced consequent to the incorporation of OVs. Liu et al.'s study [25] delineates the initiation of structural defects and lattice distortions in Co_xN_y through metal doping, a process that exerts a profound influence on the electronic structure and the adsorption dynamics of hydrogen atoms. Emerging evidence suggests a direct interrelationship between strain magnitude and the effective mass of charge carriers, an interaction that further bears implications for carrier dynamics [26]. Consequently, the exploration of strain degree effects on photocatalytic performance represents a compelling research avenue. Nonetheless, the quest to induce high-degree strain in photocatalysts via point defects presents significant challenges, because of the low strain levels induced by point defects.

In this work, we synergistically amalgamate two distinct point defect types, OVs and indium doping, which can induce opposite strains, thereby facilitating the generation of locally high-degree strain in Bi_2MoO_6 . The introduction of OVs produces tensile strain [21], while the incorporation of In^{3+} engender compressive strain in the crystal lattice of Bi_2MoO_6 . The interplay between these two zero-dimensional defects precipitates the formation of one-dimensional dislocation defects, consequently engendering pronounced three-dimensional lattice distortions. Comprehensive characterizations and photocatalytic assessments elucidate that the augmentation of local lattice strain substantially bolsters carrier separation and the genesis of surface-active sites. The optimally tailored catalyst manifests a markedly enhanced proficiency in the photocatalytic degradation of antibiotics. This work underscores the pivotal role of lattice strain in modulating photocatalytic properties, provides crucial insights for strain engineering strategies in photocatalysts.

2. Experimental section

2.1. Chemical reagent

All reagents are analytically pure and do not require further purification. Detailed reagent information can be found in the [Table S1](#).

2.2. Synthesis of Indium doped Bi_2MoO_6 with OVs

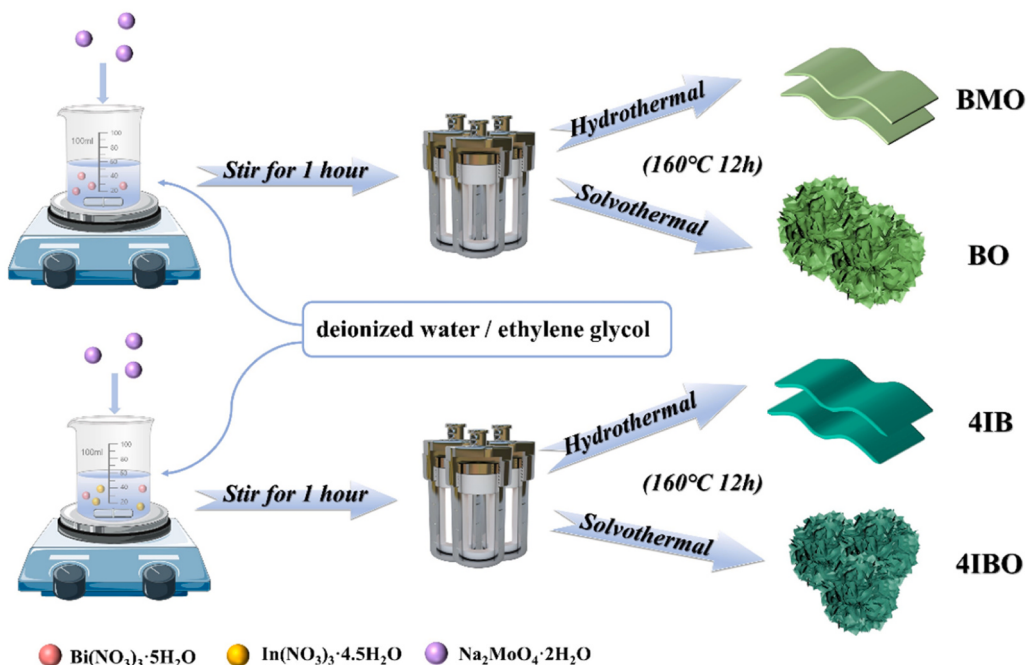
Indium-doped Bi_2MoO_6 with OVs were synthesized via a one-step solvothermal method. The synthesis process involved the dissolution of 1.5 mmol of $\text{Bi}(\text{NO}_3)_3 \cdot 5\text{H}_2\text{O}$ along with varying quantities of $\text{In}(\text{NO}_3)_3 \cdot 4.5\text{H}_2\text{O}$ (2 mol%, 4 mol%, or 6 mol%) in 50 mL of ethylene glycol (EG). Subsequently, 0.75 mmol of $\text{Na}_2\text{MoO}_4 \cdot 2\text{H}_2\text{O}$ was introduced into the solution and stirred for 1 h. The resulting suspension was transferred to a 150 mL Teflon-lined stainless steel autoclave and subjected to a 12 h heating process at 160 °C. After natural cooling of the reactor, the obtained yellow-green precipitates were centrifuged with deionized water and ethanol several times, and dried at 60 °C. The synthesized materials were assigned abbreviated names: 2%, 4%, and 6% In-doped Bi_2MoO_6 were designated as 2IBO, 4IBO, and 6IBO, respectively. In addition, the following nomenclature was adopted: initial Bi_2MoO_6 (BMO), In-doped Bi_2MoO_6 without OVs (IB), and Bi_2MoO_6 with OVs but without doping (BO). The detailed synthesis procedures can be found in the supplementary materials. [Scheme 1](#)

2.3. Characterization

The instrument information required for characterization was displayed in the [supporting materials](#).

2.4. Photocatalytic degradation tests

The assessment of photocatalytic activity involved a sequence of degradation reactions targeting tetracycline (TC), ciprofloxacin (CIP), oxytetracycline (OTC), and norfloxacin (NFX). These reactions were carried out under the irradiation of a 300 W xenon lamp fitted with a cut-off filter ($\lambda \geq 400$ nm). The procedure commenced with the preparation of TC (15 mg/L), CIP (10 mg/L), OTC (10 mg/L), or NFX (10 mg/



Scheme 1. Schematic illustration of the synthesis process for BMO, 4IB, BO, and 4IBO.

L) solutions, to which 10 mg of the photocatalyst was added. Prior to the photodegradation reaction, dark adsorption was performed under magnetic stirring for 30 min in the absence of light to establish an equilibrium between adsorption and desorption. Subsequently, the xenon lamp was activated to initiate the photodegradation process. Throughout the illumination period, at 10 min intervals, solution samples were extracted, approximately 3 mL each time. The solution samples contaminated with the target compounds were subsequently filtered using a 0.22 μm filter head. The concentration of the filtrate containing the contaminants was assessed via a UV-visible spectrophotometer (Shimadzu, UV-2450).

3. Results and discussion

3.1. Structure and composition

The investigation focused on assessing the influence of OVs and doping on the crystal structure of Bi_2MoO_6 through XRD analysis. As depicted in Fig. 1a, the diffraction peaks of all samples at 28.2°, 32.6°, 33.1°, 46.7°, 47.1°, 55.5°, 56.2°, and 58.4° corresponded to (131), (200), (210), (202), (260), (331), (191), and (262) lattice planes of Bi_2MoO_6 (JCPDS No. 84-0787) [27], respectively. No impurity peaks were detected, affirming the successful synthesis of the sample and confirmation of its high purity. Comparing the OVs-containing sample BO with the initial BMO, a marginal shift of the (131) diffraction peak toward smaller angles was evident, as depicted in Fig. 1a. This shift

towards lower angles signified an expansion of the lattice due to the influence of OVs in bulk phase, which aligns with prior findings [28]. In contrast, the diffraction peaks of the indium-doped samples exhibited a discernible shift towards larger angles, indicating a reduction in lattice size. This shift can be attributed to the introduction of indium (In^{3+} ion) into the lattice, where the smaller radius of the In^{3+} ion (94 pm) contrasts with that of the Bi^{3+} ion (103 pm) [29]. The magnitude of diffraction peak shift correspondingly increased with higher levels of indium doping, further underscoring the relationship between this shift and the introduction of indium ions. Moreover, corresponding absorption peaks were observed in Fourier transform infrared spectroscopy (FT-IR) in Fig. S1. Among them, the peak at 565.9 cm^{-1} belongs to the stretching and deformation vibration of $\text{Bi}-\text{O}$, and the spectral band at 731.7 cm^{-1} belongs to the asymmetric stretching vibration of O atoms in $\text{O}-\text{Mo}-\text{O}$ in MoO_6 octahedra, corresponding to the Mo-O stretching vibration at 844.3 cm^{-1} [30]. The successful synthesis of the catalyst was confirmed by the XRD results.

XPS analysis was implemented to delve into the intricate chemical composition and surface electronic states of the photocatalysts. As depicted in Fig. 1b, the emergence of $\text{In} 3d$ peaks corroborated the successful doping of In^{3+} within the 4IB and 4IBO samples, a finding that aligns coherently with the XRD outcomes presented in Fig. 1a. In Fig. 1c, the BMO sample revealed characteristic peaks at 159.01 and 164.31 eV, associated respectively with the $\text{Bi} 4f_{5/2}$ and $\text{Bi} 4f_{7/2}$ states. Relative to BMO, the $\text{Bi} 4f$ peaks in the 4IBO exhibited shift towards lower binding energy. Similarly, the $\text{Mo} 3d$ peaks in the 4IBO displayed a slight shift

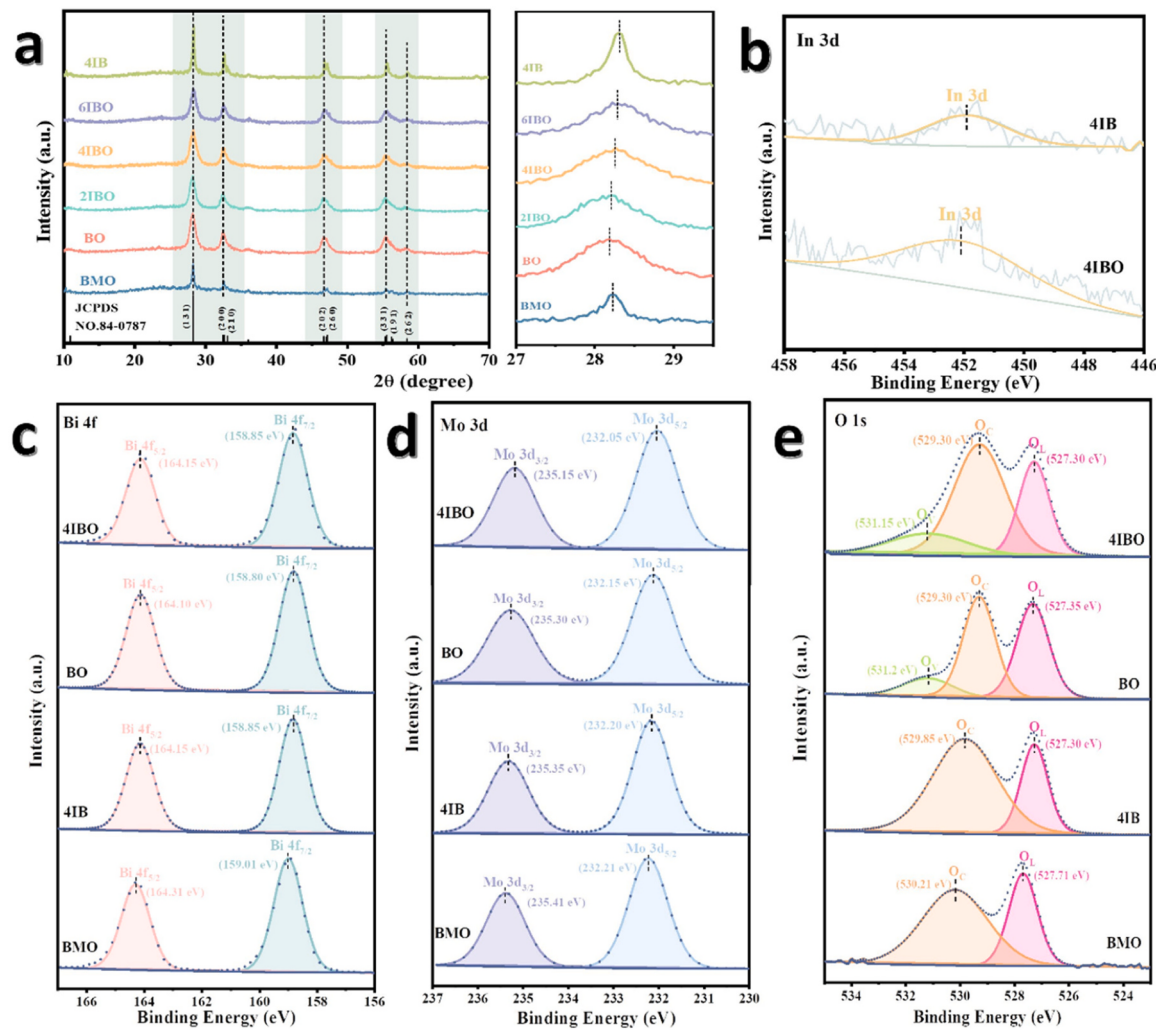


Fig. 1. (a) X-ray diffraction patterns of the as-prepared samples; The high resolution XPS spectra of In (b), Bi (c), Mo (d), and O (e) for BMO, 4IB, BO, and 4IBO.

towards lower binding energy (Fig. 1d). The decrement in binding energy for Bi and Mo suggests a subtle reduction in the valence states in 4IBO, likely attributed to the presence of OVs and doping. Fig. 1e delineated an asymmetrical peak for the O 1 s, decomposable into three peaks corresponding to lattice oxygen, adsorbed oxygen, and OVs, respectively. Different with BMO and 4IB, BO and 4IBO showed peaks attributed to OVs at around 531.20 eV, signifying the successful introduction of OVs.

3.2. Morphological analysis

As depicted in Fig. 2a-b, BMO exhibited a thick sheet-like structure with a diameter of approximately 600 nm and a thickness of about 50 nm. A marked transformation in morphology was evident in BO (Fig. 2c-d) and 4IBO (Fig. 2e-f) compared to BMO. BO adopted a

nanosphere configuration formed through the aggregation of nanosheets, suggesting that the initial morphological change arises from the self-assembly effect induced by the ethylene glycol (EG) atmosphere. This peculiar morphology could be attributed to the high viscosity of EG and the steric hindrance effect [31]. In contrast to BO, the nanosheets of 4IBO were smaller, culminating in a hairball-like structure. This indicated that, owing to indium doping, the nanoparticle size of BO was further reduced, possibly attributed to the suppression of grain growth facilitated by indium doping. In summary, the synergistic influence of OVs and indium ion doping in 4IBO resulted in a smaller particle size. This alteration can contribute to outstanding adsorption and degradation effects, along with improved catalytic performance.

TEM analysis can provide additional insights into the morphology and structure of the samples. BO (Figs. 2h and 2j) and 4IBO (Fig. 2k) hierarchical spheres were composed of numerous small nanosheets [32].

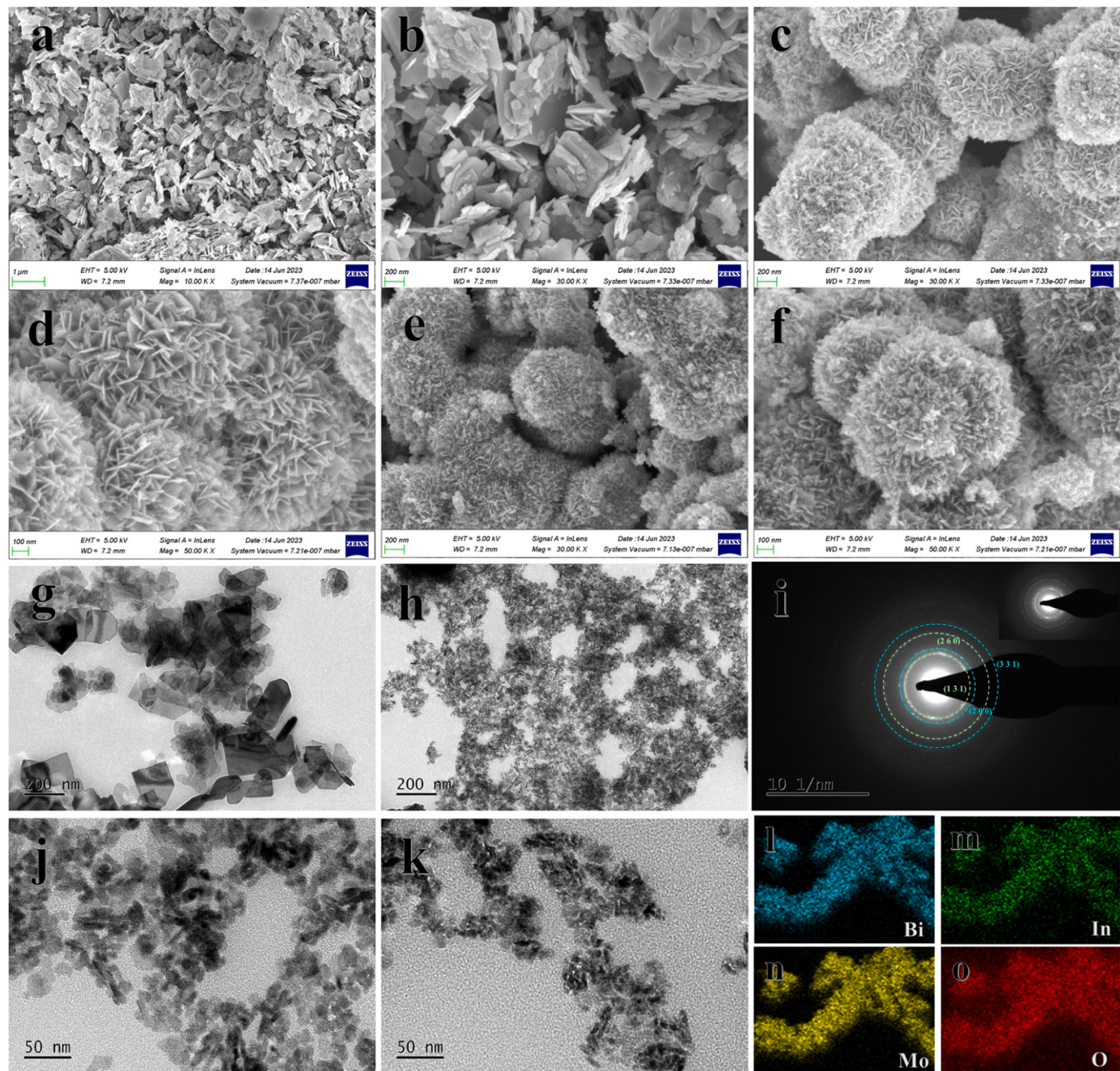


Fig. 2. SEM images of the BMO (a-b), BO (c-d), and 4IBO (e-f); TEM images of the BMO (g), BO (h and j), and 4IBO (k); SAED (i) and elemental mapping (l-o) of 4IBO.

For ease of comparison at the same magnification size, images of BMO (Fig. 2g) and BO (Fig. 2h), BO (Fig. 2j), and 4IBO (Fig. 2k) were juxtaposed, with 4IBO exhibiting a more refined structure than BO and BMO, consistent with SEM findings. The Selected Area Electron Diffraction (SAED) pattern in Fig. 2i exhibited diffraction ring radii of 0.315, 0.274, 0.192, and 0.165 nm, corresponding to crystal plane spacings of (131), (200), (260), and (331), respectively. This alignment was in harmony with the peak positions observed in XRD. The comprehensive SAED view is depicted in the upper right corner of Fig. 2i. Furthermore, Fig. 2l-o displays the EDS element distribution maps, illustrating the abundant and uniform dispersion of Bi, Mo, In, and O elements. The SAED and EDS results affirm the successful synthesis of indium-doped Bi_2MoO_6 .

The lattice structures of BMO and 4IBO nanosheets were meticulously examined through High-Resolution Transmission Electron

Microscopy (HRTEM) images. As illustrated in Fig. 3a, 4IBO revealed a conspicuous presence of lattice defects, manifested in the disruption of lattice fringes within the pink line area, indicative of lattice disorder. This occurrence stemmed from the synergistic interplay of doping and vacancies, inducing unsaturated coordination and thereby leading to the defects [33]. Notably, the HRTEM image in Fig. 3a, particularly the blue area, disclosed lattice strain induced by dislocations, further expounded upon in Fig. 3b. The displayed crystal fringes here corresponded to the (131) crystal plane, influenced by strain to expand the partial spacing from 0.316 nm to 0.320 nm [34].

Additionally, Geometric Phase Analysis (GPA) was employed to scrutinize the lattice strain distribution. Fig. 3c and h depicted the HRTEM images of BMO and 4IBO with the zone axis of <010>. The modified 4IBO exhibited noticeable lattice shrinkage compared to BMO

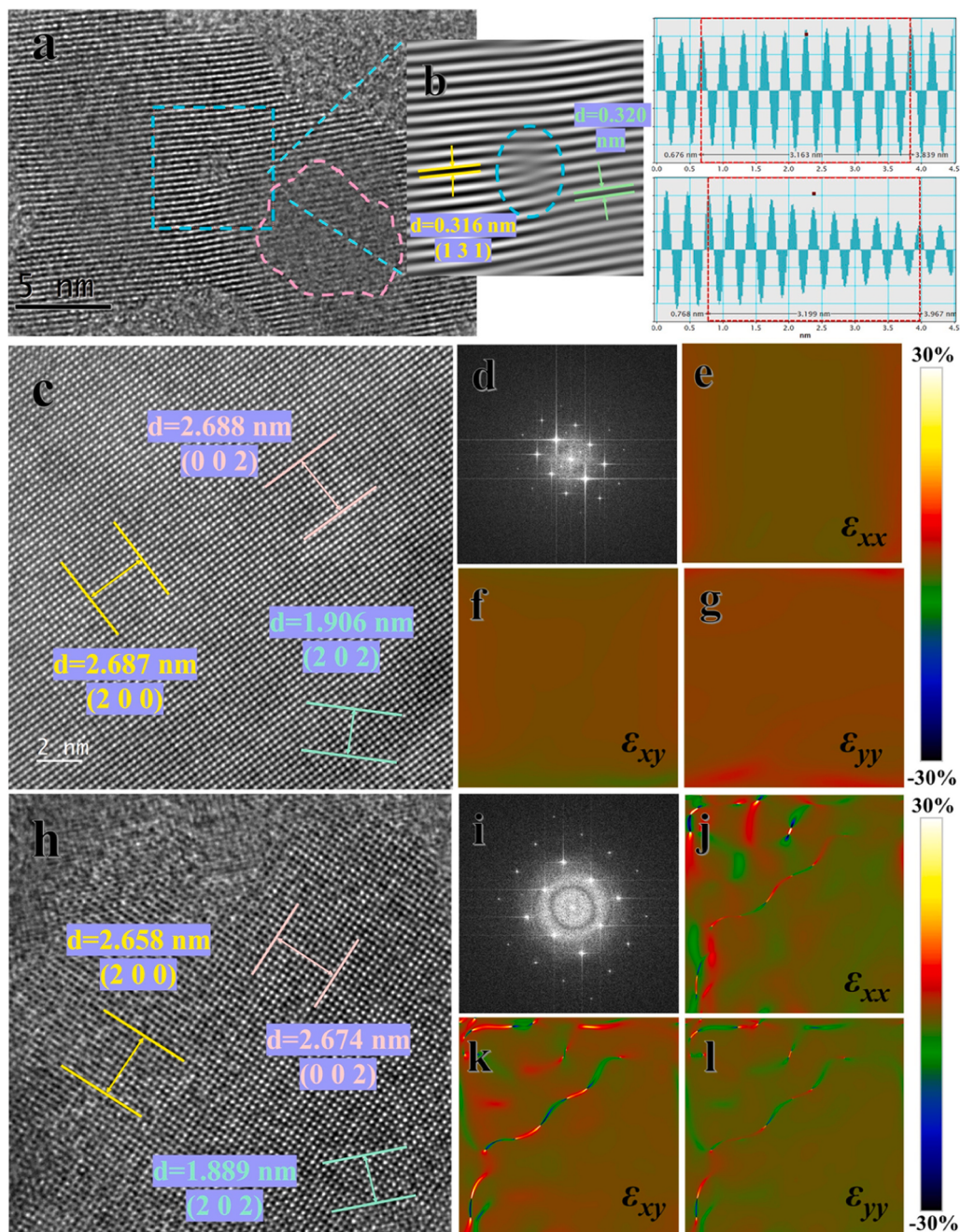


Fig. 3. (a) HRTEM image of 4IBO; (b) Inverse fast Fourier transform (IFFT) and lattice spacing profile image of the select area in (a); HRTEM images of BMO (c) and 4IBO (h); Fast Fourier transform (FFT) and GPA analysis results of BMO (d-g) and 4IBO (i-l).

overall, in line with the results of XRD peak shifts (Fig. 1a). The GPA plots in Fig. 3e-g and j-l were derived from corresponding HRTEM images of Fig. 3c and h. The internal strain in BMO appeared relatively uniform and mild, whereas 4IBO exhibited significant strain in the lattice. Lattice strain can lead to a smaller grain size, increased active sites, improved adsorption performance, and enhanced charge carrier separation [35], providing advantageous implications for augmenting catalytic performance.

3.3. Optical and photoelectrochemical properties

To comprehensively affirm the presence of OVs, electron paramagnetic resonance (EPR) measurements were conducted to scrutinize unpaired electrons harboring paramagnetism in BMO, 4IB, BO, and 4IBO catalysts, as depicted in Fig. 4a. Observations revealed an almost negligible signal from BMO and 4IB at room temperature, contrasting with a notably intensified signal in BO and 4IBO. This heightened signal intensity in 4IBO strongly suggested the successful introduction of oxygen defects [36].

Fig. 4b illustrated the photocurrent responses of BMO, 4IB, BO, and 4IBO after five repeated switching cycles under simulated sunlight illumination. The 4IBO demonstrated a heightened photocurrent response, suggesting enhanced separation and migration of photo-generated carriers [37]. The photoluminescence (PL) spectra excited at 300 nm were investigated and presented in Fig. 4c. Similarly, the PL intensity of 4IBO was the lowest at 468 nm, indicating that compared to BMO, 4IBO significantly enhances the separation and migration of charge carriers, which was consistent with the photocurrent response results. The kinetics of carrier lifetimes of BMO, 4IB, BO, and 4IBO samples were further recorded by time-resolved transient fluorescence absorption spectra (TR-PL). The fluorescence lifetimes of BMO, 4IB, BO, and 4IBO were measured to be 2.94 ns, 3.38 ns, 4.66 ns, and 11.71 ns (Fig. 4d), respectively. The TR-PL results indicated that the synergistic effect of indium doping and OVs effectively inhibited the rapid recombination of charge carriers and prolonged the lifetime of charge carriers. In Fig. 4e, the electrochemical impedance spectrum (EIS) revealed the

minimum impedance arc radius for 4IBO, and its equivalent circuit fitting was performed (inset of Fig. 4e, Table S2), which signifying the facilitated interface electron transfer. In addition, a sharp increase in the surface photovoltage of the 4IBO catalyst was detected, indicating high efficiency in charge transfer to the surface (Fig. 4f) [38]. These findings collectively indicate that the presence of strain effectively enhances the separation and migration of charge carriers, consequently diminishing the recombination efficiency of photogenerated charge carriers.

Ultraviolet-visible diffuse reflectance spectroscopy (UV-vis DRS) was employed to assess the optical characteristics of the samples. As depicted in Fig. 5a, the absorption edge of pristine BMO was identified at approximately 490 nm, signifying its responsiveness in the visible light region. The absorption edge of the modified sample shows an apparent red shift in the visible light region. When the indium doping amount is 4%, the maximum response light range was 517 nm. It may be assigned to the formation of shallow trap surfaces on the catalyst by In (III) and the relatively easy excitation of free electrons [39].

Generally, the Tauc's band gap (E_g) curves of the sample (Fig. 5b) can be calculated from the Kubelka-Munk equation in Eq. (1):

$$(\alpha h\nu)^{\frac{1}{n}} = A(h\nu - E_g)^{\#} \quad (1)$$

Among them, the symbol α , ν , A , E_g , and n represent the absorption coefficient, Planck constant, optical frequency, proportionality constant, semiconductor band gap, and semiconductor index, respectively. It is worth mentioning that the value of n is closely related to the semiconductor type, where $n=1/2$ represents direct semiconductors and $n=2$ corresponds to indirect semiconductors. Due to Bi_2MoO_6 being an indirect semiconductor, the value of n was taken as 2 [40]. Following the Tauc's plot curve as a tangent, the bandgap of BMO was determined to be 2.28 eV. After modification, the band gap of 4IBO narrowed to 1.96 eV. The specific positions of the conduction band and valence band were calculated based on the Mott-Schottky curve. As inferred from the curve in Fig. 5c, Bi_2MoO_6 is an n-type semiconductor, with the flat band positions of BMO and 4IBO being -0.28 V and -0.76 V, respectively, corresponding to E_{CB} values of -0.08 V and -0.56 V. Using the formula

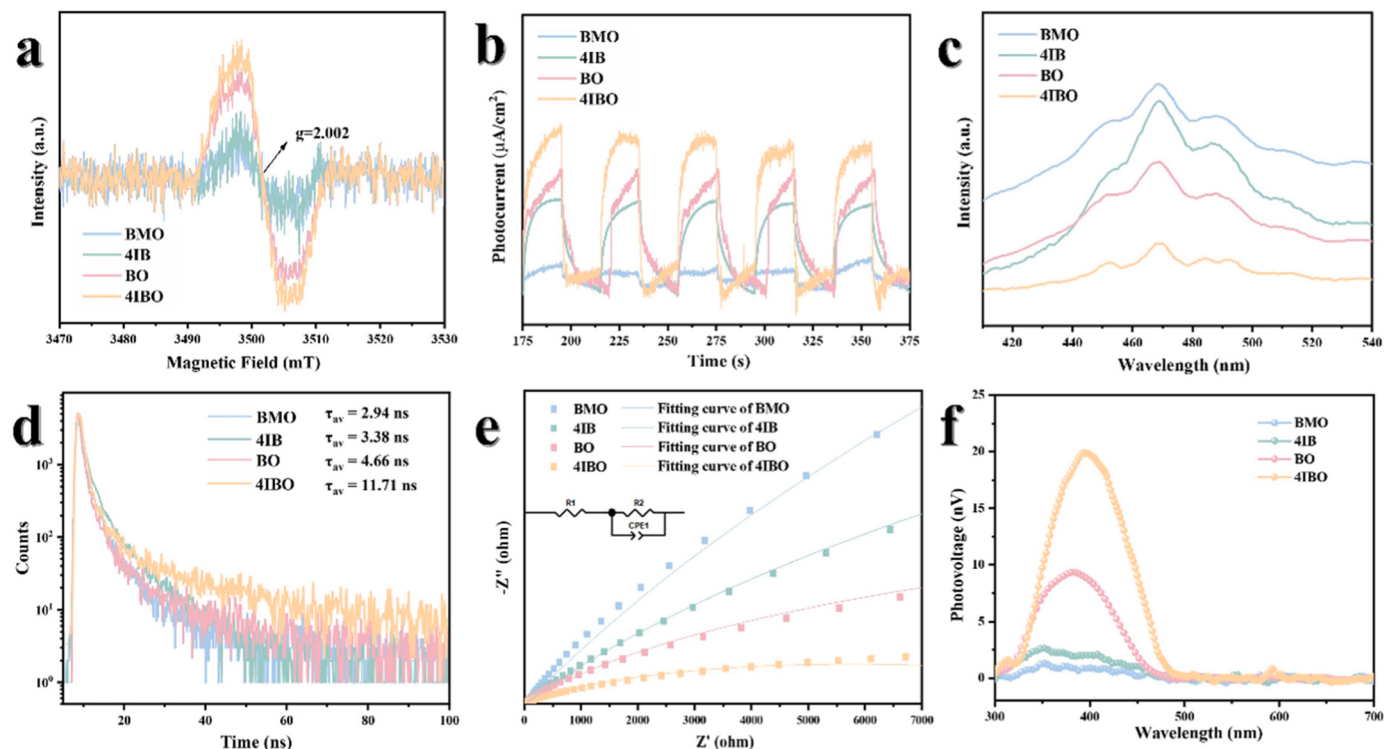


Fig. 4. EPR (a), transient photocurrent responses (b), PL (c), time-resolved PL (d), EIS (e), and surface photovoltage spectra (f) of BMO, 4IB, BO, and 4IBO.

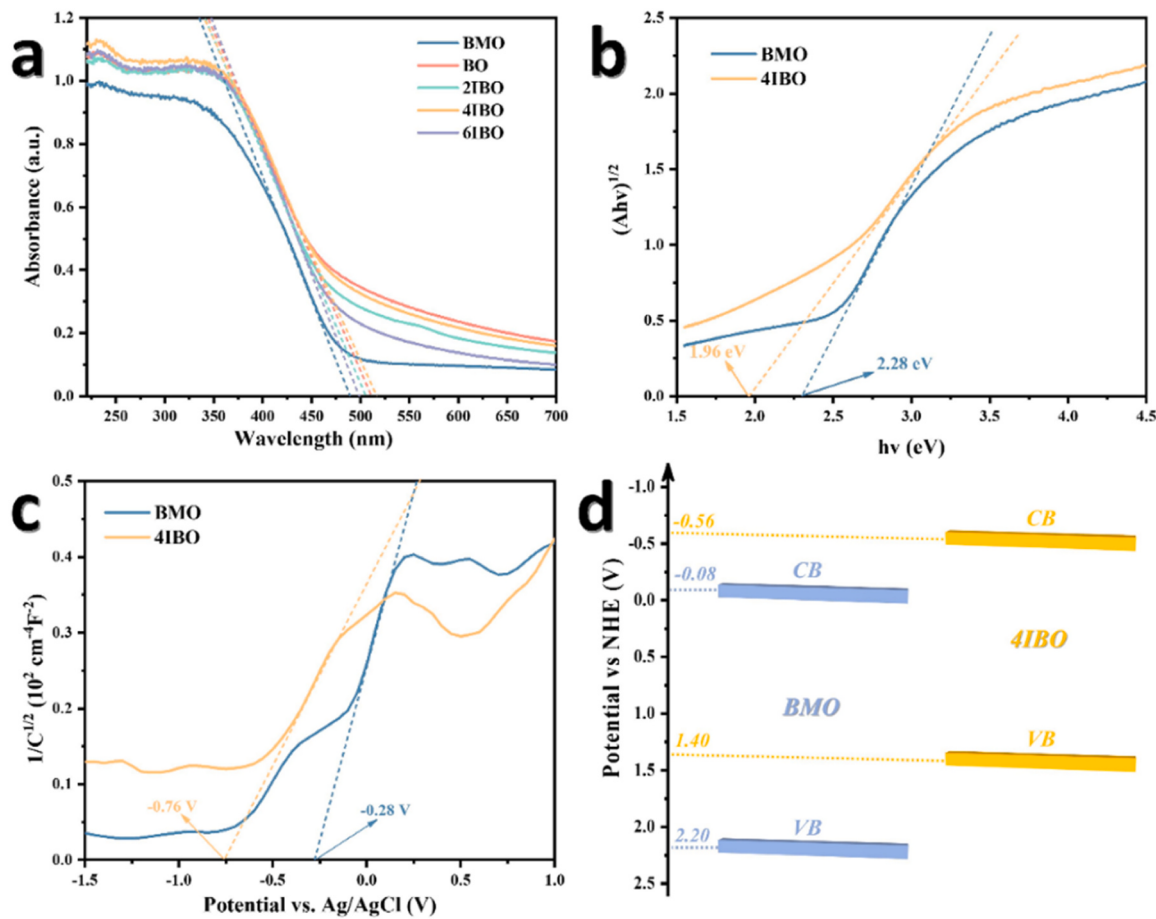


Fig. 5. (a) UV-vis diffuse reflectance spectra of samples; Tauc's plots curves (b), Mott-Schottky curves (c), and the band structure diagrams (d) of BMO and 4IBO.

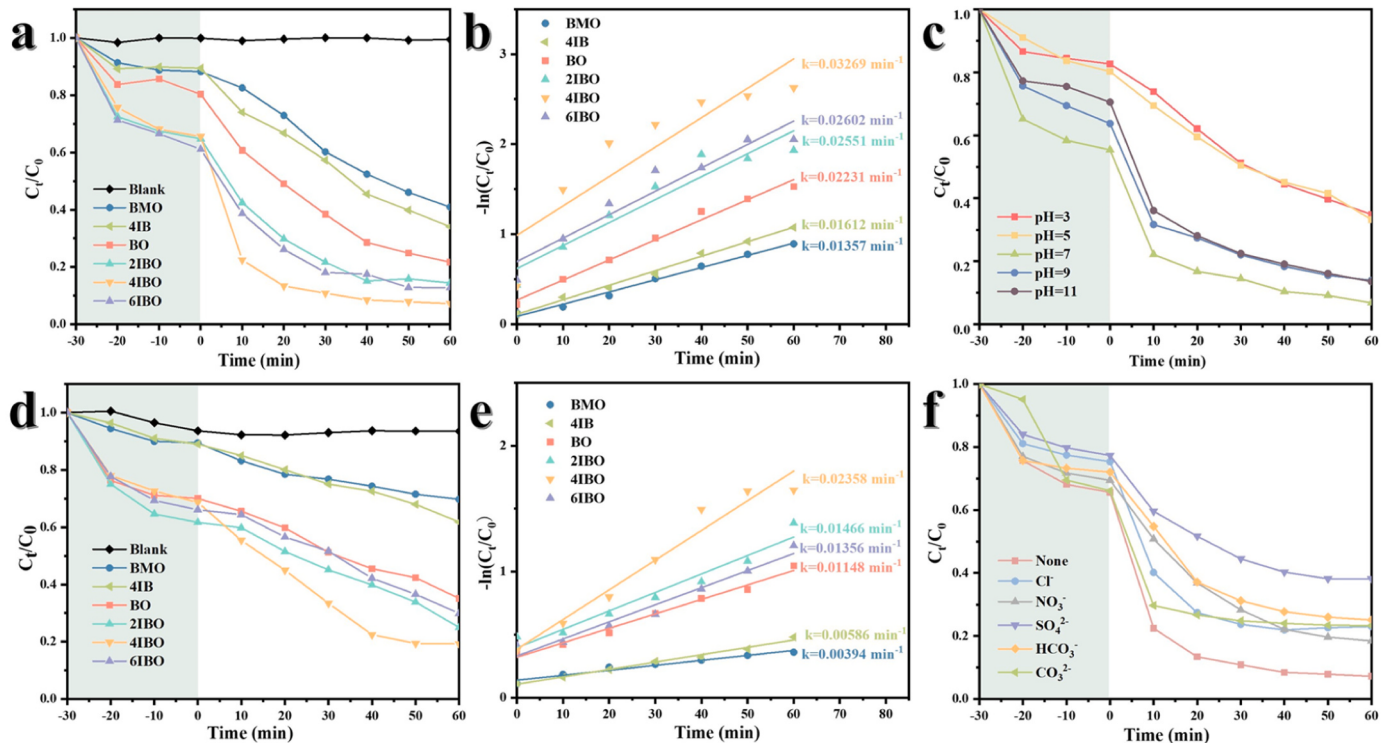


Fig. 6. Photocatalytic curves of catalysts degrading TC (a) and CIP (d) under visible light irradiation; Photocatalytic kinetics of TC (b) and CIP (e) degradation; (c) Effects of different pH values on the degradation of TC by 4IBO; (f) The effect of different ions on the degradation of TC by 4IBO.

$E_g = E_{VB} - E_{CB}$, the EVB values of BMO and 4IBO were determined as 2.20 V and 1.40 V, respectively [39]. The change in the bandgap suggested that strain could adjust the band structure, thereby enhancing the utilization of visible light [20]. The band structures of BMO and 4IBO, as deduced from the results of UV-vis DRS and Mott-Schottky analysis, were depicted in Fig. 5d. The upshifted of CB may be attributed to energy level repulsion and lattice strain [41].

3.4. Photocatalytic performances

To delve deeper into the impact of doping and OVs on photocatalytic performance, tetracycline (TC) was selected as the primary antibiotic pollutant (Fig. 6a). The variations in TC concentration (C_t/C_0) under visible light irradiation were meticulously observed. Additionally, the removal efficacy of the catalysts for ciprofloxacin (CIP) (Fig. 6d), oxytetracycline (OTC) (Fig. S2a), and norfloxacin (NFX) (Fig. S2c) was also assessed. Before the irradiation, the suspension was magnetically stirred in the dark for half an hour to attain adsorption-desorption equilibrium. The results of dark adsorption presented in Fig. 6a revealed a conspicuous augmentation in the adsorption capacity of 2IBO, 4IBO, and 6IBO compared to other catalysts, demonstrating the pivotal role of lattice strain in significantly enhancing the adsorption capacity of catalysts.

Blank experiments indicated that TC was stable under visible light irradiation. The catalyst BMO exhibited a mere 59.06% degradation rate of TC after 60 min of irradiation, which was attributed to its weak visible light absorption and rapid recombination of photogenerated charge carriers. Following the introduction of indium ion doping or OVs, the degradation rates increased to 65.88% (4IB) and 78.30% (BO), respectively. The synergistic interaction of the doping and OVs in 4IBO resulted in an impressive TC removal rate of 93.19%, signifying a substantial enhancement in degradation efficiency. The degradation efficiency of 2IBO and 6IBO were 85.53% and 87.17%, respectively. This improvement is likely attributed to the existence of strain induced by OVs and doping, markedly enhancing the mobility of photocatalytic active electrons and holes. Furthermore, the removal trends of CIP, OTC, and NFX by the catalysts mirrored those of TC. The removal rates for CIP were in the order: 4IBO (81.68%) > 2IBO (75.00%) > 6IBO (70.07%), and for OTC: 4IBO (72.98%) > 6IBO (68.45%) > 2IBO (67.00%). The removal rates of NFX were as follows: 4IBO (78.80%) > 6IBO (72.21%) > 2IBO (64.04%).

Due to the varying adsorption capacities of photocatalysts, pseudo-first-order kinetic models were employed to analyze the degradation results of TC (Fig. 6b), CIP (Fig. 6e), OTC (Fig. S2b), and NFX (Fig. S2d). As shown in Eq. (2):

$$-\ln \frac{C_t}{C_0} = k_{ap} t \quad (2)$$

C_t , C_0 , t , and k_{ap} are the concentration of the target contaminant, the initial concentration of TC (CIP, OTC, or NFX), the reaction time, and the reaction rate constant, respectively, after the reaction t min. All catalysts exhibited general adherence to the pseudo-first-order kinetic model. Notably, in the degradation processes of TC, CIP, OTC, and NFX, the degradation rates for 4IBO were 2.41, 5.98, 1.63, and 18.27 times higher than those for BMO, respectively.

In real wastewater scenarios, the pH value plays a crucial role in influencing the photocatalytic activity. The degradation efficiency of TC under various initial pH conditions has been depicted in Fig. 6c. The introduction of diluted NaOH solution resulted in a slight decrease in the photocatalytic degradation rate of TC. When adapting to acidic conditions using HNO_3 , the degradation efficiency sharply declined. This phenomenon could be attributed to the conversion of TC to its cationic form in acidic media ($\text{pH} < 7$). The existing forms of TC molecules under different pH conditions have been listed in Table S3 [42].

Chloride ions, sulfate ions, carbonate ions, nitrate ions, and bicarbonate ions are ubiquitous anions in natural water and exert an

inevitable impact on the practical efficacy of photocatalysis [43]. Hence, it is imperative to scrutinize the influence of major ions on pollutant degradation by catalysts. As depicted in Fig. 6f, the experiment introduced NaCl , Na_2CO_3 , Na_2HCO_3 , Na_2SO_4 , and NaNO_3 at a concentration of 0.1 mol/L to assess their impact on the photodegradation of TC by 4IBO. The findings ultimately revealed that anions can impede the degradation of TC, with the effect of inorganic ions on the removal rate of TC following this sequence: $\text{NO}_3^- < \text{Cl}^- < \text{CO}_3^{2-} < \text{HCO}_3^- < \text{SO}_4^{2-}$. The addition of Cl^- resulted in a degradation efficiency decrease to 76.97%, attributed to the competitive adsorption surface between Cl^- and TC on the catalyst. As CO_3^{2-} and HCO_3^- act as free radical scavengers [44], their inclusion moderately diminishes the removal efficiency of TC. Following the addition of SO_4^{2-} , the removal rate of TC significantly declined (61.87%). The presence of SO_4^{2-} markedly impacted the photocatalytic degradation of TC negatively, as it generated by consuming $\cdot\text{OH}$ to form $\cdot\text{SO}_4^{2-}$. Conversely, when NO_3^- was added, the degradation efficiency was 81.56%, indicating that NO_3^- had minimal influence on the catalytic degradation of TC compared to other anions. The primary ionic reactions that might occur are detailed in Table S4 [45].

3.5. Intermediates and toxicity analysis

The degree of mineralization of the tetracycline solution was quantified by measuring total organic carbon (TOC). The 4IBO catalyst demonstrated a significantly higher mineralization efficiency compared to BMO, BO, and 4IB (Fig. S3a). However, the degree of mineralization (58.9%) was lower than the degradation efficiency, suggesting that not all tetracycline molecules were fully mineralized into H_2O and CO_2 , but were instead partially decomposed into intermediates.

To substantiate the hypothesized photodegradation pathway of TC, the LC-MS spectrometer was employed to detect the intermediates generated throughout the degradation process. Integrating the findings from Figs. S4-S6 and existing literature analyses, four potential pathways were delineated in Fig. 7. For Pathway I, the conversion of TC to P1 ($m/z=467$) was instigated by the hydrogenation of the $\text{C}=\text{O}$ double bond and the subsequent addition of hydroxyl groups [46]. In the second pathway [44], the dehydration of the hydroxyl group situated on C6 in TC, due to its inherent instability, led to the formation of an ene. Subsequently, the tertiary amine of C4 removed the two methylene groups, resulting in the generation of P2 ($m/z=399$). Upon ROS attack, the acyl amino group of P2 was detached, giving rise to P3 ($m/z=362$). The carbon atom ring of P3 can be dissociated, leading to the production of P4 ($m/z=318$). Persistent attack from active free radicals induced further decomposition of P4, culminating in the formation of P5 ($m/z=274$). Pathway III involved the conversion of the TC molecule ($m/z=445$) to P6 ($m/z=417$) through the separation of two methyl groups on the tertiary amine [47]. P7 ($m/z=265$) and P8 ($m/z=239$) were generated through the cleavage of double carbon bonds and the detachment of amino and carbonyl groups. The final step involved the achievement of P9 ($m/z=182$) through a ring-opening reaction and the loss of methylene [48]. Additionally, the formation process of P10 ($m/z=318$) and P11 ($m/z=182$) included hydroxylation, N-dealkylation, and dehydration reactions [49]. Ultimately, through the oxidation of free radicals, the intermediate will continue to undergo mineralization, converting into CO_2 , H_2O , and other inorganic ions.

To elucidate the practical implications of 4IBO photocatalytic samples in the degradation of TC, we assessed the acute toxicity (Fathead minnow LC_{50} , $\text{Daphnia magna LC}_{50}$), developmental toxicity, and mutagenicity of TC and its degradation intermediates using the Toxicity Estimation Software Tool (T.E.S.T.). The software relies on quantitative structure-activity relationship analysis, providing a comprehensive exploration of the toxicity associated with TC and its derivatives. From Fig. 8a, it can be observed that compared to TC, the LC_{50} values of P1 and P10 fat headed fish increased, while in P2 and P6, an opposite trend was observed. Remarkably, the LC_{50} value of P2 remained relatively stable even after further oxidation (P3, P4, P5). Most TC intermediates

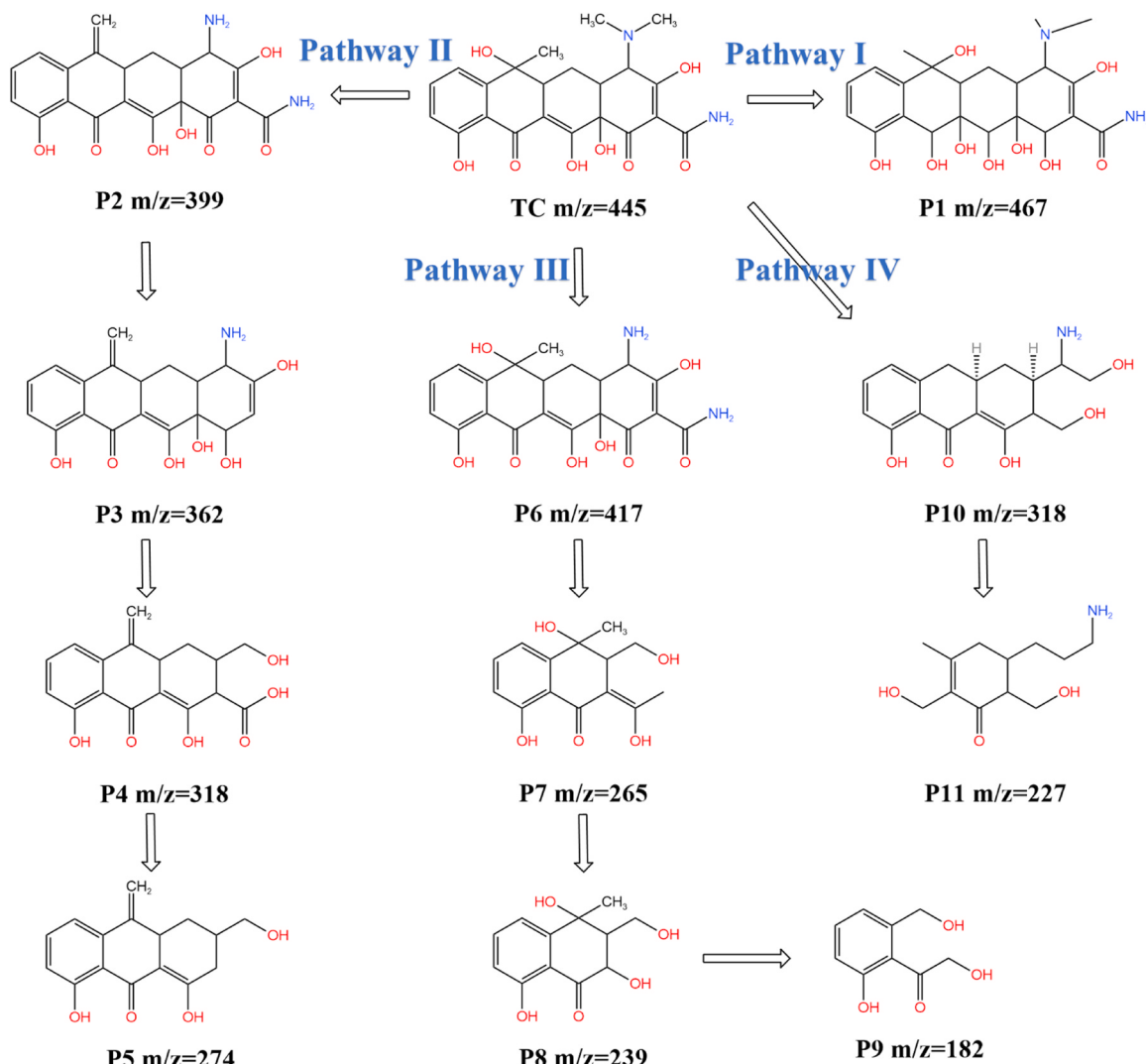


Fig. 7. The proposed degradation pathways of TC by 4IBO.

exhibited significantly higher LC₅₀ values compared to TC, indicating an overall reduction in acute toxicity. The trends in *Daphnia magna* LC₅₀ and *Fathead minnow* LC₅₀, as depicted in Fig. 8b, were generally consistent. Fig. 8c revealed a substantial reduction in developmental toxicity for most intermediates within the 4IBO system after a series of conversions. In Fig. 8d, TC, initially categorized as mutagenicity positive, exhibited a decrease in mutagenicity values for P8, P9, and P11 to "mutagenicity negative" as the photocatalytic reaction progressed. The data used for toxicity evaluation by the T.E.S.T. software was presented in Table S5. Although some intermediates still displayed residual toxicity according to the toxicity predictions, their degradation could be achieved by prolonging the reaction time, thus reducing the overall toxicity of TC. In summary, the TC photodegradation facilitated by 4IBO contributes to the transformation of intermediates, resulting in a reduction in their biological toxicity.

Additionally, to validate the practical application of TC removal with 4IBO, we cultivated 150 mung beans in deionized water, TC-degraded with 4IBO, and a 15 mg/L TC solution for 7 days. Evaluate the impact of mung beans on organisms based on their germination rate and growth length distribution at room temperature. Fig. S3b illustrates that all mung beans sprouted. The sprouts cultured in a 15 mg/L TC solution exhibited stem lengths below 4 cm, predominantly distributed between 2 and 3 cm. Deionized water and TC treated with 4IBO showed similar distribution patterns, with sprouts having stems longer than 4 cm

accounting for 32% and 28%, respectively. This indicates a significant inhibitory effect of TC on bean sprout growth, and the degradation treatment with 4IBO markedly improved the growth environment and condition of bean sprouts.

3.6. Possible mechanism analysis

The reusability and stability of the 4IBO structure were systematically evaluated through cyclic experiments aimed at degrading TC. As shown in Fig. 9a, even after five consecutive cycles, the TC removal rate maintained a high level of 85.06%, marking only an 8.13% decrease from the initial degradation rate. XRD, SEM, TEM, and XPS analyses were conducted to characterize and compare their properties before and after use (Fig. S7). No significant differences in morphology and structure were observed compared to the initial sample, attesting to the 4IBO had outstanding stability and sustained photocatalytic activity.

To elucidate the primary active species responsible for TC degradation and delineate the mechanism underlying the 4IBO photocatalytic degradation of TC, radical capture experiments were systematically conducted. The experimental protocol involved introducing 0.01 g of 4IBO into a 50 mL TC solution for a 30 min adsorption period under dark conditions. Subsequently, capture agents, namely 4-Hydroxy-TEMPO (TEMPOL), isopropanol (IPA), disodium ethylenediaminetetraacetic acid (EDTA-2Na), and furfuryl alcohol (FFA), were introduced to

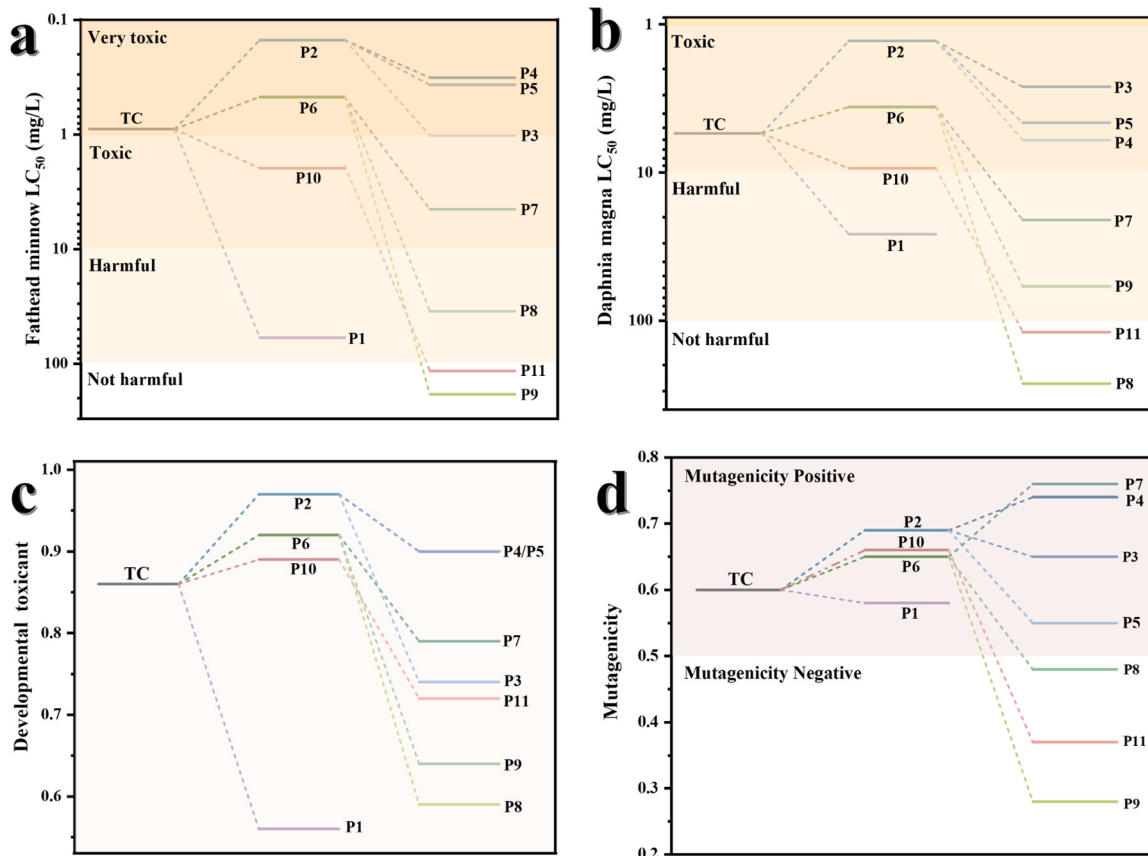
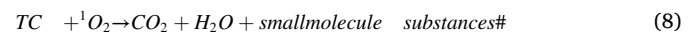
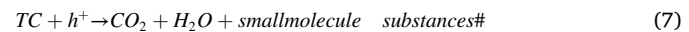
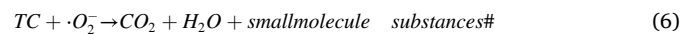
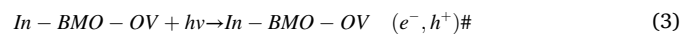


Fig. 8. The acute toxicity of Fathead minnow LC₅₀ (a), Daphnia magna LC₅₀ (b), developmental toxicant (c), and mutagenicity (d) of TC.

the solution to selectively capture $\cdot\text{O}_2$, $\cdot\text{OH}$, h^+ , and $^1\text{O}_2$, respectively. The outcomes, as depicted in Fig. 9b revealed notable trends. Particularly, EDTA-2Na exhibited the most pronounced impact on the TC removal rate, with the active species captured by EDTA-2Na identified as h^+ , signifying that h^+ stands as the principal active species in the degradation of TC. Furthermore, the addition of FFA led to a substantial inhibitory effect on TC removal, indicating that $^1\text{O}_2$ also represents a key active species in the degradation of TC. Introduction of TEMPOL moderately inhibited the degradation rate of photocatalytic 4IBO, suggesting that $\cdot\text{O}_2$ contributes as an auxiliary active species. Conversely, the addition of IPA induced only a marginal decrease in the removal rate of TC, implying that, during the photocatalytic process, the influence of $\cdot\text{OH}$ is relatively modest. Additionally, the presence of $\cdot\text{O}_2$ and $^1\text{O}_2$ was further confirmed through electron spin resonance (ESR) under illumination. Fig. 9c and d displayed the peak intensity signals of typical superoxide radicals ($\cdot\text{O}_2$) and singlet oxygen ($^1\text{O}_2$), which was consistent with the results of the radical capture experiment.

Building upon the outcomes of the conducted experiments, we put forth a prospective photocatalytic mechanism for 4% In-doped Bi₂MoO₆ with OVs (4IBO), driven by the strain engendered through the collaborative influence of OVs and doping (refer to Fig. 10). The postulated mechanism posits potential pathways through which 4IBO engages in the degradation of TC:



Under visible light irradiation, the generation of photogenerated carriers in Bi₂MoO₆ results from the excitation of light energy, causing valence band electrons to migrate to the conduction band, leaving behind positive holes (h^+). The introduction of vacancies in Bi₂MoO₆ serves to broaden the absorption range of light, thereby enhancing the utilization of photons. Concurrently, surface capture traps induced by indium doping capture photogenerated electrons, mitigating the recombination rate of these electrons and holes to some extent. Furthermore, the lattice strain, arising from the synergistic effect of vacancies and doping, induces the formation of local built-in electric fields, significantly improving the transport dynamics of charge carriers [50]. Electrons interact with dissolved oxygen in water to generate $\cdot\text{O}_2$, and subsequently, $\cdot\text{O}_2$ reacts with holes, further yielding $^1\text{O}_2$ [51,52]. Through redox reactions involving $\cdot\text{O}_2$, $^1\text{O}_2$, and h^+ , TC undergoes successful degradation, ultimately transforming into inorganic substances such as H₂O and CO₂ [53].

4. Conclusion

In summary, we have successfully synthesized indium-doped Bi₂MoO₆ with incorporated OVs using a straightforward one-step solvent thermal precipitation method. The resultant 4IBO manifests efficient charge separation capabilities and heightened light absorption efficiency, showcasing exceptional performance in the photodegradation of organic pollutants. Utilizing XRD, SEM, and TEM analyses, we have substantiated that the introduction of OVs results in the size reduction and agglomeration of nanosheets, with additional indium ions contributing to a further reduction in the grain size of Bi₂MoO₆.

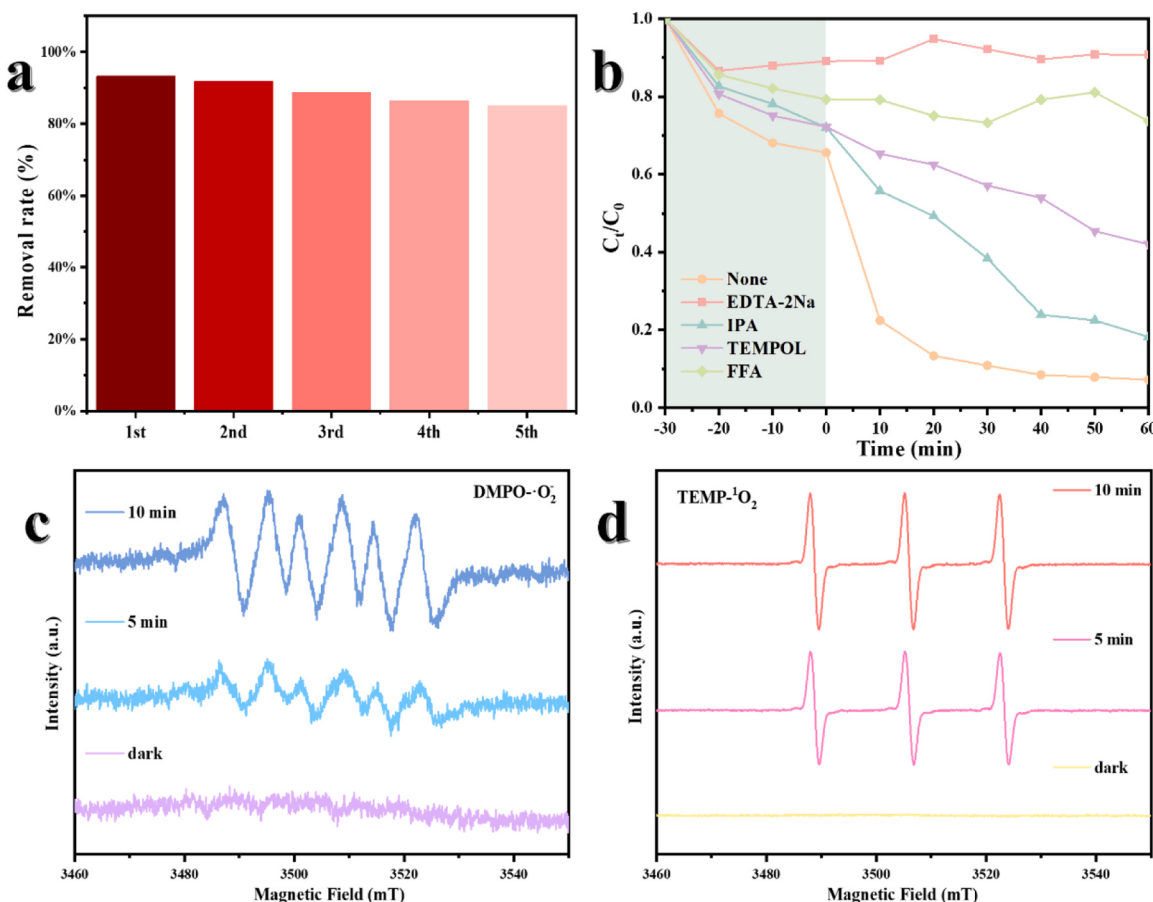


Fig. 9. (a) Cycling experiments of TC degradation by 4IBO; (b) The trapping experiments of reactive species in the degradation of TC by 4IBO; $\cdot\text{O}_2$ (c) and $^1\text{O}_2$ (d) ESR patterns of 4IBO.

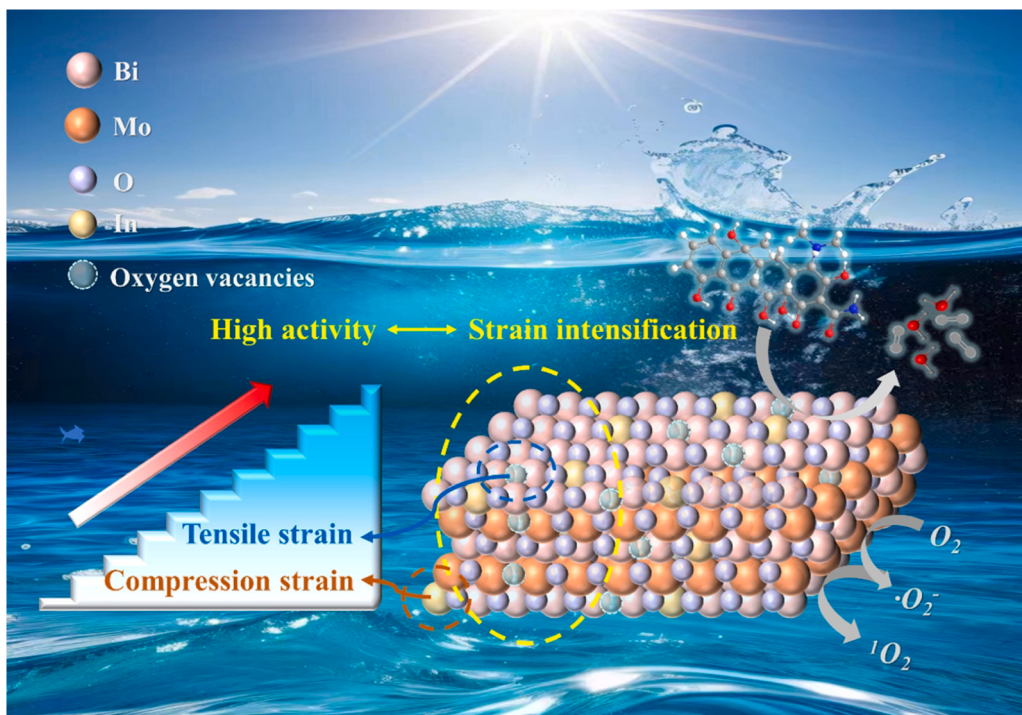


Fig. 10. Proposed photocatalytic mechanism of In^{3+} doping Bi_2MoO_6 containing oxygen vacancies.

HRTEM and GPA analyses have revealed that 4IBO undergoes lattice strain, leading to increased active sites and improved adsorption performance, advantageous for catalytic enhancement and carrier separation. The investigation into the impact of strain arising from the synergistic effect on photodegradation performance has been exhaustive. Experimental results highlight that 4IBO exhibits remarkable photocatalytic activity in the degradation of TC, CIP, OTC, and NFX, achieving rates of 93.19%, 81.68%, 72.98%, and 78.80%, respectively, within a 60 min span of visible light irradiation. This performance surpasses degradation rates of pristine Bi_2MoO_6 by 2.41, 5.98, 1.63, and 18.27 times, respectively. The elucidation of cleavage pathways for TC molecules was proposed via LC-MS detection, and the assessment of the toxicity of diverse intermediate molecules was conducted. Our study furnishes valuable insights into nanocomposites with the synergistic effects of metal doping and OVs, laying the groundwork for optimizing bismuth-based catalysts to modulate photocatalysts for superior catalytic performance.

CRediT authorship contribution statement

Xinyue Chang: Writing – review & editing, Writing – original draft, Software, Investigation, Data curation. **Qishe Yan:** Supervision, Resources, Methodology, Funding acquisition. **Yan-Yang Li:** Writing – review & editing, Supervision, Resources, Methodology, Conceptualization. **Yanan Cheng:** Validation, Formal analysis, Conceptualization. **Zhiyuan Guo:** Validation, Methodology, Formal analysis. **Jiayu Liu:** Validation, Formal analysis.

Declaration of Competing Interest

The authors declare that they have no known competing financial interests or personal relationships that could have appeared to influence the work reported in this paper.

Data Availability

Data will be made available on request.

Acknowledgements

This work was supported by the Henan Provincial Department of Science and Technology (grant number: 202102310266).

Appendix A. Supporting information

Supplementary data associated with this article can be found in the online version at [doi:10.1016/j.apcatb.2024.123858](https://doi.org/10.1016/j.apcatb.2024.123858).

References

- [1] C. Li, C. Song, H. Li, L. Ye, Y. Xu, Y. Huang, G. Nie, R. Zhang, W. Liu, N. Huang, P. K. Wong, T. Ma, Ultradurable fluorinated V_2AlC for peroxymonosulfate activation in organic pollutant degradation processes, *Chin. J. Catal.* 43 (2022) 1927–1936.
- [2] M. Cai, Y. Liu, C. Wang, W. Lin, S. Li, Novel $\text{Cd}_{0.5}\text{Zn}_{0.5}/\text{Bi}_2\text{MoO}_6$ S-scheme heterojunction for boosting the photodegradation of antibiotic enrofloxacin: Degradation pathway, mechanism and toxicity assessment, *Sep. Purif. Technol.* 304 (2023) 122401.
- [3] A.J. Browne, M.G. Chipeta, G. Haines-Woodhouse, E.P.A. Kumaran, B.H. K. Hamadani, S. Zaraa, N.J. Henry, A. Deshpande, R.C. Reiner, Jr, N.P.J. Day, A. D. Lopez, S. Dunachie, C.E. Moore, A. Stergachis, S.I. Hay, C. Dolecek, Global antibiotic consumption and usage in humans, 2000–18: a spatial modelling study, *Lancet Planet. Health* 5 (2021) 893–904.
- [4] Q. Yuan, S. Qu, R. Li, Z.Y. Huo, Y. Gao, Y. Luo, Degradation of antibiotics by electrochemical advanced oxidation processes (EAOPs): Performance, mechanisms, and perspectives, *Sci. Total Environ.* 856 (2023) 159092.
- [5] X. Liang, B. Chen, X. Nie, Z. Shi, X. Huang, X. Li, The distribution and partitioning of common antibiotics in water and sediment of the Pearl River Estuary, South China, *Chemosphere* 92 (2013) 1410–1416.
- [6] N. Nasrollahi, L. Ghalamchi, V. Vatanpour, A. Khataee, Photocatalytic-membrane technology: a critical review for membrane fouling mitigation, *J. Ind. Eng. Chem.* 93 (2021) 101–116.
- [7] Y. Zhang, J. Zhou, W. Cai, J. Zhou, Z. Li, Enhanced photocatalytic performance and degradation pathway of Rhodamine B over hierarchical double-shelled zinc nickel oxide hollow sphere heterojunction, *Appl. Surf. Sci.* 430 (2018) 549–560.
- [8] M. Hamandi, G. Berhault, C. Guillard, H. Kochkar, Reduced graphene oxide/ TiO_2 nanotube composites for formic acid photodegradation, *Appl. Catal. B: Environ.* 209 (2017) 203–213.
- [9] C. Wang, R. Yan, M. Cai, Y. Liu, S. Li, A novel organic/inorganic S-scheme heterostructure of TCPP/ $\text{Bi}_{12}\text{O}_{17}\text{Cl}_2$ for boosting photodegradation of tetracycline hydrochloride: Kinetic, degradation mechanism, and toxic assessment, *Appl. Surf. Sci.* 610 (2023) 155346.
- [10] X. Liu, S. Gu, Y. Zhao, G. Zhou, W. Li, BiVO_4 , Bi_2WO_6 and Bi_2MoO_6 photocatalysis: a brief review, *J. Mater. Sci. Technol.* 56 (2020) 45–68.
- [11] K. Liu, L. Wang, T. Fu, H. Zhang, C. Lu, Z. Tong, Y. Yang, Y. Peng, Oxygen-functionalized Ti_3C_2 MXene/exfoliated montmorillonite supported S-scheme $\text{BiOBr}/\text{Bi}_2\text{MoO}_6$ heterostructures for efficient photocatalytic quinolone antibiotics degradation, *Chem. Eng. J.* 457 (2023) 141271.
- [12] Z. Li, Z. Wu, S. Zhang, J. Shen, W. Feng, Y. Du, L. Wan, S. Zhang, Defect state of indium-doped bismuth molybdate nanosheets for enhanced photoreduction of chromium(vi) under visible light illumination, *Dalton Trans.* 47 (2018) 8110–8120.
- [13] S.N. Lou, J. Scott, A. Iwase, R. Amal, Y.H. Ng, Photoelectrochemical water oxidation using a $\text{Bi}_2\text{MoO}_6/\text{MoO}_3$ heterojunction photoanode synthesised by hydrothermal treatment of an anodised MoO_3 thin film, *J. Mater. Chem. A* 4 (2016) 6964–6971.
- [14] Y. Ma, Y. Jia, L. Wang, M. Yang, Y. Bi, Y. Qi, Exfoliated thin Bi_2MoO_6 nanosheets supported on WO_3 electrode for enhanced photoelectrochemical water splitting, *Appl. Surf. Sci.* 390 (2016) 399–405.
- [15] J. Yang, T. Xie, Y. Mei, J. Chen, H. Sun, S. Feng, Y. Zhang, Y. Zhao, J. Wang, X. Li, J. He, H. Chen, High-efficiency V-Mediated Bi_2MoO_6 photocatalyst for PMS activation modulation of energy band structure and enhancement of surface reaction, *Appl. Catal. B: Environ.* 339 (2023) 123149.
- [16] T. Ma, C. Yang, L. Guo, R.A. Soomro, D. Wang, B. Xu, F. Fu, Refining electronic properties of Bi_2MoO_6 by In-doping for boosting overall nitrogen fixation via relay catalysis, *Appl. Catal. B: Environ.* 330 (2023) 122643.
- [17] C. Yang, Y. Zhang, F. Yue, R. Du, T. Ma, Y. Bian, R. Li, L. Guo, D. Wang, F. Fu, Co doping regulating electronic structure of Bi_2MoO_6 to construct dual active sites for photocatalytic nitrogen fixation, *Appl. Catal. B: Environ.* 338 (2023) 123057.
- [18] G. Wang, T. Huo, Q. Deng, F. Yu, Y. Xia, H. Li, W. Hou, Surface-layer bromine doping enhanced generation of surface oxygen vacancies in bismuth molybdate for efficient photocatalytic nitrogen fixation, *Appl. Catal. B: Environ.* 310 (2022) 121319.
- [19] Z. Zafar, S. Yi, J. Li, C. Li, Y. Zhu, A. Zada, W. Yao, Z. Liu, X. Yue, Recent development in defects engineered photocatalysts: an overview of the experimental and theoretical strategies, *Energy Environ. Mater.* 5 (2021) 68–114.
- [20] Y. Miao, Y. Zhao, S. Zhang, R. Shi, T. Zhang, Strain engineering: a boosting strategy for photocatalysis, *Adv. Mater.* 34 (2022) e2200868.
- [21] B. Huang, Y. Liu, Q. Pang, X. Zhang, H. Wang, P.K. Shen, Boosting the photocatalytic activity of mesoporous SrTiO_3 for nitrogen fixation through multiple defects and strain engineering, *J. Mater. Chem. A* 8 (2020) 22251–22256.
- [22] S. Zhang, Y. Zhao, R. Shi, C. Zhou, G.I.N. Waterhouse, L.Z. Wu, C.H. Tung, T. Zhang, Efficient photocatalytic nitrogen fixation over $\text{Cu}^{\delta+}$ -modified defective ZnAl -layered double hydroxide nanosheets, *Adv. Energy Mater.* 10 (2020) 1901973.
- [23] Y. Zhao, Y. Zhao, G.I.N. Waterhouse, L. Zheng, X. Cao, F. Teng, L.Z. Wu, C.H. Tung, D. O'Hare, T. Zhang, Layered-double-hydroxide nanosheets as efficient visible-light-driven photocatalysts for dinitrogen fixation, *Adv. Mater.* 29 (2017) 1703828.
- [24] Y. Zhao, Y. Zhao, R. Shi, B. Wang, G.I.N. Waterhouse, L.Z. Wu, C.H. Tung, T. Zhang, Tuning Oxygen Vacancies in Ultrathin TiO_2 Nanosheets to boost photocatalytic nitrogen fixation up to 700 nm, *Adv. Mater.* 31 (2019) e1806482.
- [25] S. Liu, W. Qi, J. Liu, X. Meng, S. Adimi, J.P. Attfield, M. Yang, Modulating electronic structure to improve the solar to hydrogen efficiency of cobalt nitride with lattice doping, *ACS Catal.* 13 (2023) 2214–2222.
- [26] Y. Chen, Y. Lei, Y. Li, Y. Yu, J. Cai, M.H. Chiu, R. Rao, Y. Gu, C. Wang, W. Choi, H. Hu, C. Wang, Y. Li, J. Song, J. Zhang, B. Qi, M. Lin, Z. Zhang, A.E. Islam, B. Maruyama, S. Dayeh, L.J. Li, K. Yang, Y.H. Lo, S. Xu, Strain engineering and epitaxial stabilization of halide perovskites, *Nature* 577 (2020) 209–215.
- [27] P. Ju, Y. Zhang, L. Hao, J. Cao, K. Dou, F. Jiang, C. Sun, Facile in-situ construction of plate-on-plate structured $\text{Bi}_2\text{MoO}_6/\text{BiO}$ Z-scheme heterojunctions enriched with oxygen vacancies for highly efficient photocatalytic performances, *Appl. Surf. Sci.* 602 (2022) 154319.
- [28] K. Qian, Y. Yan, S. Xi, T. Wei, Y. Dai, X. Yan, H. Kobayashi, S. Wang, W. Liu, R. Li, Elucidating the strain–vacancy–activity relationship on structurally deformed $\text{Co}@\text{CoO}$ nanosheets for aqueous phase reforming of formaldehyde, *Small* 17 (2021) 2102970.
- [29] T.B.O. Nunes, M.D. Teodoro, M.R.D. Bomio, F.V. Motta, Photocatalytic degradation of methylene blue and dye mixture using indium-doped CaWO_4 synthesized by sonochemical and microwave-assisted hydrothermal methods, *Dalton Trans.* 51 (2022) 18234–18247.
- [30] C. Wang, M. Cai, Y. Liu, F. Yang, H. Zhang, J. Liu, S. Li, Facile construction of novel organic–inorganic tetra (4-carboxyphenyl) porphyrin/ Bi_2MoO_6 heterojunction for tetracycline degradation: Performance, degradation pathways, intermediate toxicity analysis and mechanism insight, *J. Colloid Interface Sci.* 605 (2022) 727–740.

[31] C. Guan, T. Hou, W. Nie, Q. Zhang, L. Duan, X. Zhao, Enhanced photocatalytic reduction of CO_2 on BiOBr under synergistic effect of Zn doping and induced oxygen vacancy generation, *J. Colloid Interface Sci.* 633 (2023) 177–188.

[32] C. Liu, Y. Ren, Z. Wang, Y. Shi, B. Guo, Y. Yu, L. Wu, Flowerlike BiOCl nanospheres fabricated by an *in situ* self-assembly strategy for efficiently enhancing photocatalysis, *J. Colloid Interface Sci.* 607 (2022) 423–430.

[33] H. Qin, J. Sun, D. Xia, H. Xu, Q. Yu, Y. Zheng, Y. Shi, Boosting nonradical process in BiOI/BiOCl heterostructure by interface oxygen vacancies, *Chem. Eng. J.* 435 (2022) 134847.

[34] X. Cao, A. Huang, C. Liang, H.-C. Chen, T. Han, R. Lin, Q. Peng, Z. Zhuang, R. Shen, H.M. Chen, Y. Yu, C. Chen, Y. Li, Engineering lattice disorder on a photocatalyst: photochromic BiOBr nanosheets enhance activation of aromatic C–H bonds via water oxidation, *J. Am. Chem. Soc.* 144 (2022) 3386–3397.

[35] X. Zhang, L. Hui, D. Yan, J. Li, X. Chen, H. Wu, Y. Li, Defect rich structure activated 3D palladium catalyst for methanol oxidation reaction, *Angew. Chem. Int. Ed.* 62 (2023) e202308968.

[36] X. Li, G. Dong, F. Guo, P. Zhu, Y. Huang, C. Wang, Enhancement of photocatalytic NO removal activity of $\text{g-C}_3\text{N}_4$ by modification with illite particles, *Environ. Sci. Nano* 7 (2020) 1990–1998.

[37] J. Geng, L. Zhao, M. Wang, G. Dong, W. Ho, The photocatalytic NO -removal activity of $\text{g-C}_3\text{N}_4$ significantly enhanced by the synergistic effect of Pd^0 nanoparticles and N vacancies, *Environ. Sci. Nano* 9 (2022) 742–750.

[38] S. Li, L. Hou, L. Zhang, L. Chen, Y. Lin, D. Wang, T. Xie, Direct evidence of the efficient hole collection process of the CoO_x cocatalyst for photocatalytic reactions: a surface photovoltage study, *J. Mater. Chem. A* 3 (2015) 17820–17826.

[39] Q. Yan, T. Zhang, Y. Fu, Y. Zeng, C. Xu, P. Wang, X. Zhou, Nickel-Doping accelerated charge separation in flower ball-like $\text{Bi}_4\text{O}_5\text{I}_2$ for efficient visible-light photocatalytic performance, *Appl. Surf. Sci.* 540 (2021) 148310.

[40] S. Li, C. Wang, Y. Liu, M. Cai, Y. Wang, H. Zhang, Y. Guo, W. Zhao, Z. Wang, X. Chen, Photocatalytic degradation of tetracycline antibiotic by a novel $\text{Bi}_2\text{Sn}_2\text{O}_7/\text{Bi}_2\text{MoO}_6$ S-scheme heterojunction: Performance, mechanism insight and toxicity assessment, *Chem. Eng. J.* 429 (2022) 132519.

[41] X. Cai, F.P. Sabino, A. Janotti, S.-H. Wei, Approach to achieving ap-type transparent conducting oxide: doping of bismuth-alloyed Ga_2O_3 with a strongly correlated band edge state, *Phys. Rev. B* 103 (2021) 115205.

[42] D. Huang, J. Li, G. Zeng, W. Xue, S. Chen, Z. Li, R. Deng, Y. Yang, M. Cheng, Facile construction of hierarchical flower-like Z-scheme $\text{AgBr}/\text{Bi}_2\text{WO}_6$ photocatalysts for effective removal of tetracycline: Degradation pathways and mechanism, *Chem. Eng. J.* 375 (2019) 121991.

[43] C. Wu, H. Zuo, H. Du, S. Zhang, L. Wang, Q. Yan, Construction of layered embedding dual Z-Scheme $\text{Bi}_2\text{O}_2\text{CO}_3/\text{g-C}_3\text{N}_4/\text{Bi}_2\text{O}_3$: tetracycline degradation pathway, toxicity analysis and mechanism insight, *Sep. Purif. Technol.* 282 (2022) 120096.

[44] C. Wu, H. Zuo, S. Zhang, S. Zhao, H. Du, Q. Yan, A novel strategy to construct a direct Z-Scheme $\text{Bi}@\text{Bi}_2\text{O}_2\text{CO}_3/\text{g-C}_3\text{N}_4$ heterojunction catalyst via PDA electronic bridge, *Sep. Purif. Technol.* 294 (2022) 121242.

[45] H. Wu, Z. Hu, R. Liang, X. Zhang, M. Zhou, O.A. Arotiba, B-doping mediated formation of oxygen vacancies in $\text{Bi}_2\text{Sn}_2\text{O}_7$ quantum dots with a unique electronic structure for efficient and stable photoelectrocatalytic sulfamethazine degradation, *J. Hazard. Mater.* 456 (2023) 131696.

[46] H. Zuo, C. Wu, H. Du, Z. Guo, Y. Cheng, Q. Yan, Interfacial coupling of 3D nanoflower-like $\text{Bi}_2\text{O}_2\text{CO}_3$ with PANI for tetracycline photocatalytic degradation and intermediate toxicity analysis, *Appl. Surf. Sci.* 633 (2023) 157600.

[47] G. Yang, Y. Liang, Z. Xiong, J. Yang, K. Wang, Z. Zeng, Molten salt-assisted synthesis of $\text{Ce}_4\text{O}_7/\text{Bi}_4\text{MoO}_9$ heterojunction photocatalysts for Photo-Fenton degradation of tetracycline: enhanced mechanism, degradation pathway and products toxicity assessment, *Chem. Eng. J.* 425 (2021) 130689.

[48] S. Xin, S. Huo, C. Zhang, X. Ma, W. Liu, Y. Xin, M. Gao, Coupling nitrogen/oxygen self-doped biomass porous carbon cathode catalyst with $\text{CuFeO}_2/\text{biochar}$ particle catalyst for the heterogeneous visible-light driven photo-electro-Fenton degradation of tetracycline, *Appl. Catal. B: Environ.* 305 (2022) 121024.

[49] S. Mao, C. Liu, Y. Wu, M. Xia, F. Wang, P. Porous, Fe-doped $\text{g-C}_3\text{N}_4$ nanostructure with enhanced photo-Fenton activity for removal of tetracycline hydrochloride: Mechanism insight, DFT calculation and degradation pathways, *Chemosphere* 291 (2022) 133039.

[50] Y. Hu, Y. Pan, Z. Wang, T. Lin, Y. Gao, B. Luo, H. Hu, F. Fan, G. Liu, L. Wang, Lattice distortion induced internal electric field in TiO_2 photoelectrode for efficient charge separation and transfer, *Nat. Commun.* 11 (2020) 2129.

[51] K. Chu, Y. Luo, P. Shen, X. Li, Q. Li, Y. Guo, Unveiling the Synergy of O-vacancy and heterostructure over $\text{MoO}_{3-x}/\text{MXene}$ for N_2 electroreduction to NH_3 , *Adv. Energy Mater.* 12 (2021) 2103022.

[52] X. Kang, G. Dong, T. Dong, Oxygen vacancy defect engineering of heterophase junction TiO_2 : interfacial/surface oxygen vacancies coadjust the photocatalytic ROS production, *ACS Appl. Energy Mater.* 6 (2023) 1025–1036.

[53] T. Zhang, S. Zhang, C. Wu, H. Zuo, Q. Yan, Novel $\text{La}^{3+}/\text{Sm}^{3+}$ co-doped $\text{Bi}_5\text{O}_7\text{I}$ with efficient visible-light photocatalytic activity for advanced treatment of wastewater: Internal mechanism, TC degradation pathway, and toxicity analysis, *Chemosphere* 313 (2023) 137540.